Supplementary S1 - Description of the Physical Models

1. Photogeneration in Semiconductors

When a semiconductor is illuminated with photons of energy $h\nu$ (where h is Planck's constant and ν is the frequency of the incident light), electrons can be excited from the valence band to the conduction band, generating electron–hole pairs. In a conventional semiconductor framework, this process increases the concentration of non-equilibrium carriers (holes in n-type materials or electrons in p-type materials) or further increases the concentration of majority carriers if the photon energy is sufficiently large.

In COMSOL, such photogeneration is typically represented by an additional source term in the continuity equations for electrons and holes. This term is proportional to the local optical absorption and the intensity of the electromagnetic field. The generation rate G directly leads to an increase in charge carriers, and therefore to the appearance (or enhancement) of a photocurrent within the semiconductor.

2. Wave Optics and Optical Absorption

To calculate the distribution of the electromagnetic field inside the structure, the Wave Optics Module is employed. The primary governing equations are the frequency-domain form of Maxwell's equations, often expressed as a vector Helmholtz equation in terms of either the electric field E or the magnetic field H.

A key parameter is the complex dielectric function ε which can also be written in terms of the complex refractive index $n-ik$. Light absorption in the semiconductor is governed by the imaginary part of the refractive index k.

Solving Maxwell's equations provides the spatial distribution of E. In addition, COMSOL's Indirect Optical Transitions functionality can be used to model contributions to absorption that are not captured by direct transitions. The generation rate G for indirect absorption can be expressed as:

$$G = \varepsilon_0 * n * k * \frac{E_0^2}{\hbar}$$

where:

ε_0 is the permittivity of free space,

n is the real part of the refractive index,

k is the imaginary part of the refractive index,

E_0 is the local (peak) electric field amplitude,

$\hbar$ is the reduced Planck constant.

As shown, G increases with stronger local fields ($\propto E_0^2$) and with higher n.

3. Semiconductor Module and Continuity Equations

In the Semiconductor Module, the electron and hole densities (n and p) are governed by the continuity equations:

$$\frac{\partial n}{\partial t} = \frac{1}{e}\nabla J_n + G - R$$
$$\frac{\partial p}{\partial t} = \frac{1}{e}\nabla J_p + G - R$$

where:

J_n and J_p are the current densities of electrons and holes, respectively,

e is the elementary charge,

G is the carrier generation rate (including photogeneration),

R represents carrier recombination.

The Indirect Optical Transitions feature adds a generation term G to these continuity equations, thus incorporating photogeneration into the semiconductor transport calculations.

4. Drift-Diffusion Model

In the classical drift-diffusion approximation, the electron current density J_n is given by:

$$J_n = e * \mu_n * n * E + e * D_n \nabla n$$

where:

μ_n is the electron mobility,

D_n is the electron diffusion coefficient,

E is the electric field (obtained from solving Poisson's equation).

An analogous expression holds for holes:

$$J_p = e * \mu_p * p * E - e * D_p \nabla p$$

with the sign convention reflecting the positive charge of holes.

The total photocurrent in the device arises from the combined contributions of the electron and hole currents. When photogeneration increases the carrier concentrations n and p, these carriers drift under the electric field E and also diffuse toward lower concentration regions, forming the net photocurrent measurable at the device terminals.

5. Numerical Workflow

Electromagnetic Calculation: Solve Maxwell's equations to obtain the local electric field E_0 and derive n and k. From these, compute the local absorption and thus the carrier generation rate G.

Semiconductor Calculation: Solve the coupled semiconductor equations (drift-diffusion and Poisson) with the generation rate G included as a source term in the continuity equations for electrons and holes.

Current Extraction: Integrate the current density $Jn+Jp$ at the contacts (e.g., drain/source boundaries in a field-effect transistor) to obtain the total device current, which includes both dark current and photocurrent.

6. Summary

By combining the Wave Optics Module to capture the optical field distribution with the Semiconductor Module to model carrier transport and recombination, COMSOL solves a fully coupled multiphysics problem. This approach is essential for accurately predicting photogeneration in complex semiconductor structures, particularly in quasi-2D materials where light absorption and carrier dynamics can be strongly influenced by dimensional constraints, surface defects, and interference effects.

Supplementary S2 – Edge effects of electrode structures

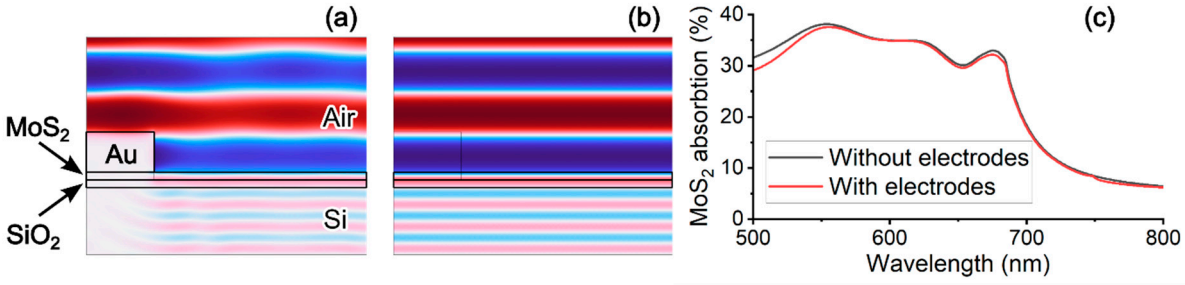


Figure S2. Dependence of optical absorption on MoS_2 thickness.

This section presents electromagnetic simulations quantifying the impact of gold electrode structures on optical absorption in the MoS_2 film. All geometric parameters were chosen to replicate Reference #20 (10.1002/adma.201201909): 60 nm MoS_2 thickness, 50 nm Al_2O_3, and 100 nm gold electrodes. Figure S2a-b shows the spatial distribution of the electric field (Ex component) for cases with and without gold electrodes at $\lambda = 400$ nm. The simulations confirm that the thick gold electrodes create complete optical shadowing, preventing direct illumination of the underlying MoS_2 film due to their opacity at this wavelength.

To quantify edge effects, we compared total absorption in the MoS_2 film for two scenarios: (1) full electrode coverage and (2) absorption only in the central electrode-free region. The difference between these values represents the contribution from electrode-edge proximity effects. Figure S2c presents the spectral dependence of this relative absorption difference. In the case without electrodes (black line), absorption was calculated for the entire film, while in the case with electrodes (red line), absorption was calculated only in the central region of the film, excluding the left and right segments covered by electrodes.

At 630 nm, edge-related absorption contributions account for less than 0.3%. This minimal edge effect results from optical shadowing by the thick, smooth electrodes, which suppresses both direct illumination and plasmonic field enhancements that could occur in nanoscale or textured electrode architectures.

These results apply specifically to the idealized planar geometry modeled here. Nanoscale electrodes or complex surface textures may exhibit stronger edge effects due to localized plasmonic resonances or subwavelength field confinement, which lie beyond the scope of this idealized model.

Supplementary S3 - Spectral dependence of optical absorption in a DPM film on its thickness.

This section discusses the dependence of optical absorption on the thickness of the TMDC layer. Figure S3.1 presents the calculated results for different pump wavelengths. It is evident that absorption varies with wavelength due to the strongly nonlinear absorption coefficient (k) of the TMDC material. However, the absorption curves as a function of thickness exhibit a complex profile, with a noticeable dip in the range of 15-40 nm. While typical absorption should follow an exponential dependence, this behavior deviates due to multi-beam interference within the transparent Al_2O_3 layer.

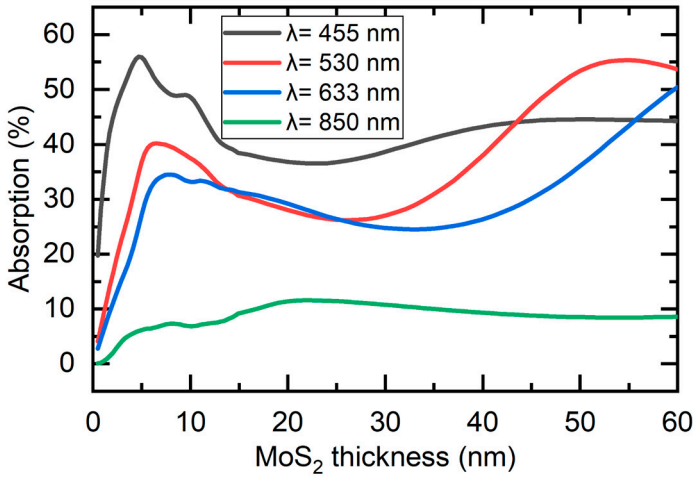


Figure S3.1. Dependence of optical absorption on MoS_2 thickness.

To confirm this effect, maps of the amplitude distribution of the electric field component of the incident optical radiation, with a wavelength of 455 nm, were generated and are shown in Figure S3.2. As observed, in the case of a monolayer substrate, a portion of the optical radiation passes entirely through the structure and even penetrates the silicon substrate. This corresponds to the leftmost point on Figure S3.1 and can be explained by the fact that light largely traverses the structure and is absorbed in the substrate. At a thickness of approximately 7 monolayers (4.8 nm), there is a sharp increase in absorption within the TMDC layer.

With further increases in thickness, the intensity of reflected radiation initially rises significantly (23 nm). Beyond this point, light can no longer penetrate the TMDC layer and is absorbed according to the Beer-Lambert law. At greater thicknesses, the dependence on thickness becomes negligible, and absorption remains constant.

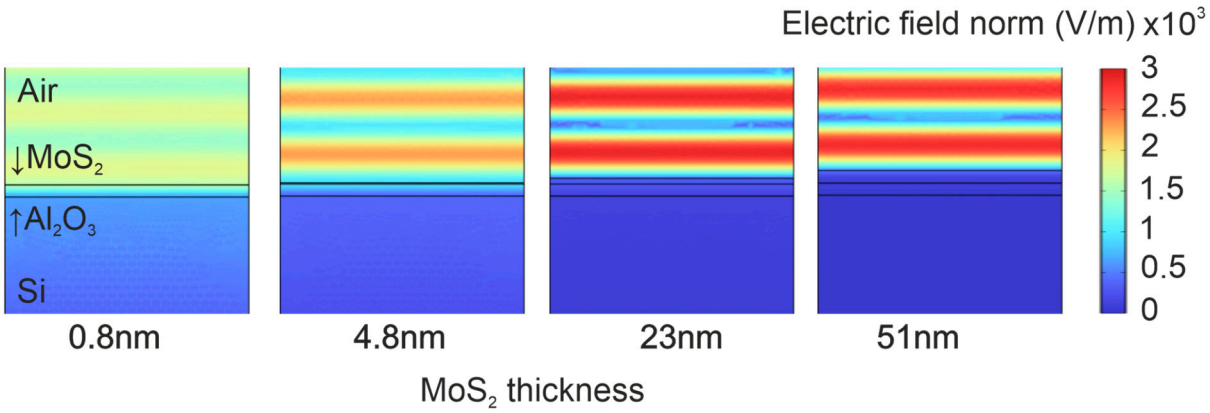


Figure S3.2. Distribution of the electric field component of optical radiation in the studied structure.

A similar model can also be employed to determine the maximum absorption at a specific wavelength or for a particular film thickness. For instance, Figure S3.3 presents a map of absorption as a function of these parameters.

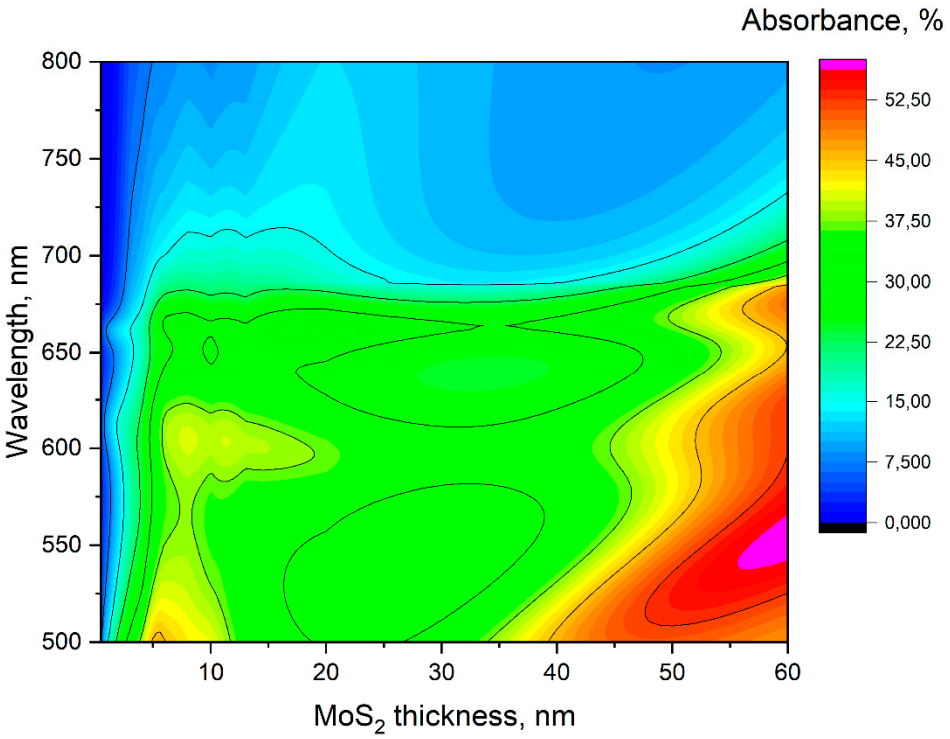


Figure S34.3. Calculated absorption maps for MoS_2 films as a function of their thickness and the wavelength of incident light.

Supplementary S4 - Contrast modelling of a two-dimensional MoS2 film.

To validate the proposed optical model, experimental and theoretical data from [Zhang, H., *Sci Rep* 5, 8440 (2015)] were utilized as a benchmark. Simulations were conducted for two geometric configurations:

1) Air/MoS_2/SiO_2/Si: A structure incorporating the two-dimensional TMDC semiconductor layer.

2) Air/SiO_2/Si: A structure without the TMDC layer.

For both configurations, reflectance curves were calculated as functions of the oxide layer thickness. All constants for the optical parameters of the materials, as well as the structural dimensions and the wavelength of the laser radiation, were directly sourced from [Zhang, H., *Sci Rep* 5, 8440 (2015)]. Using the standard formula for determining contrast between two objects, the following equation was applied:

$$Contrast = \frac{I_{substrate} - I_{MoS2}}{I_{substrate} + I_{MoS2}}$$

where $I_{substrate}$ and I_{MoS2} represent the intensities of reflected light for the two configurations. These two sets of dependencies, shown in the figure S3 (right axis).

The resulting contrast curve is shown in S4 as a red line (left axis), with the dashed black line representing the reference data. The results from our model demonstrate excellent agreement with those reported by Zhang, H. in Scientific Reports 5, 8440 (2015), even for the more complex scenario involving variable structural geometry. This consistency confirms the accuracy and reliability of the optical component of the model.

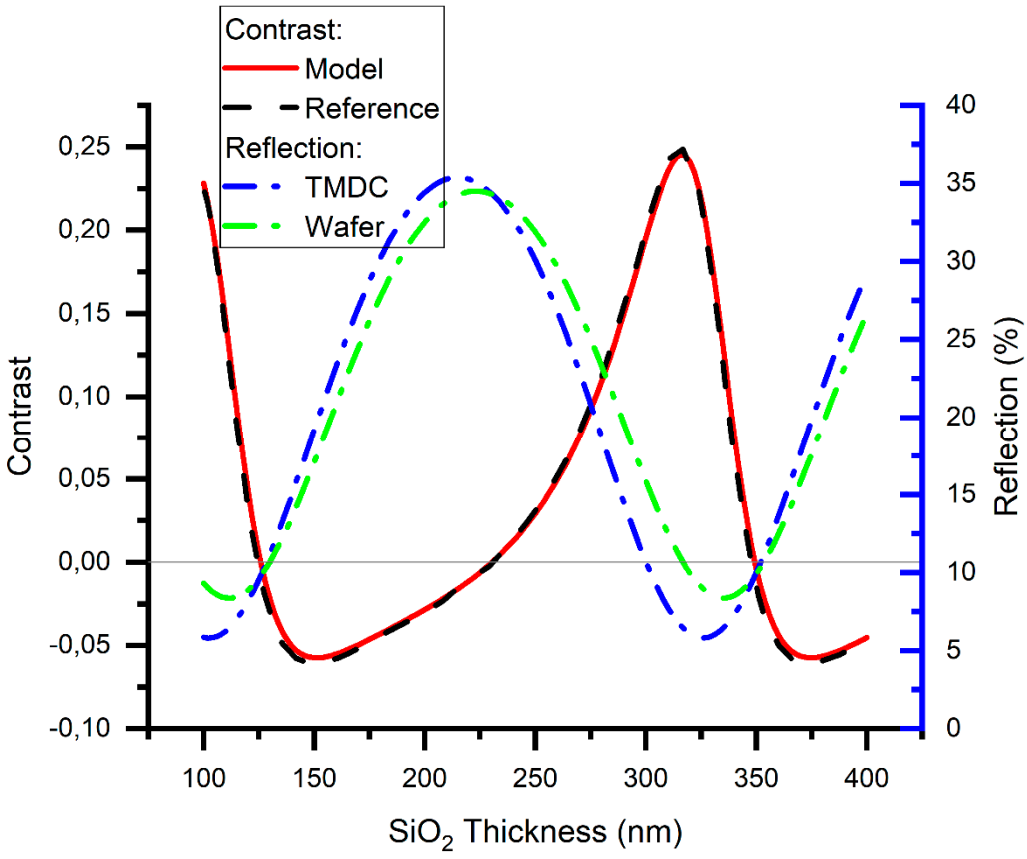


Figure S4. Simulated reflectance results for the structures Air/MoS2/SiO_2/Si (blue curve) and Air/SiO_2/Si (green curve), along with the TMDC contrast against the substrate background. The contrast (left axis) is shown for both the proposed model and the reference data from Zhang, H., Scientific Reports 5, 8440 (2015).

Supplementary S5 – Parameters of metal-semiconductor transition

Building upon the discussion of depletion region formation and Schottky barrier dynamics, the choice of metal-semiconductor junction topology critically influences the operational characteristics of photodetectors based on 2D materials. As demonstrated in Figure S5, three distinct contact regimes-ideal ohmic, thermionic Schottky, and quantum-corrected Schottky-exhibit markedly different current-voltage (I–V) behaviors.

In the ideal ohmic case, the I-V curve remains linear and symmetric across bias polarities, indicating unimpeded carrier injection at the interface. However, as shown in Figure S5, this regime only dominates under strong forward bias, while reverse bias conditions reveal a "blocking" zone where contact resistance increases sharply due to carrier depletion. Transitioning to a Schottky-type junction introduces a temperature-dependent potential barrier, which modifies the I-V characteristics through thermionic emission dynamics. The simulated saturation current in this regime aligns with Landauer's formalism for ballistic transport across narrow barriers.

A more complete treatment incorporates quantum mechanical tunneling through the thin (≤2 nm) Schottky barrier inherent to 2D materials. The WKB approximation reveals transmission probabilities exceeding 80% for carriers with energies near the conduction band edge when the depletion width approaches the Debye length (~20 nm in MoS_2). This explains why the tunneling-corrected model in Figure S5 exhibits quasi-ohmic behavior despite the nominal Schottky barrier height—a phenomenon amplified in 2D systems due to reduced dielectric screening.

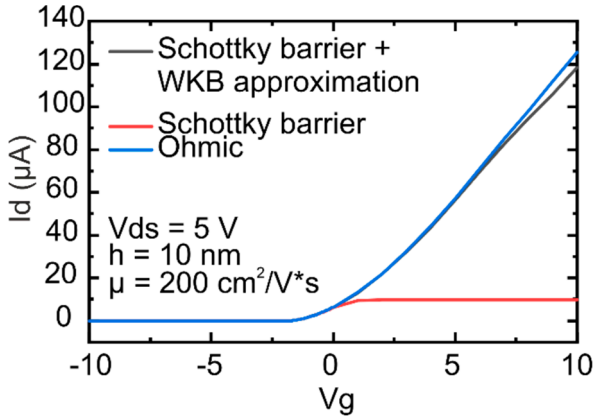


Figure S5. Id modeling results for different types of metal-semiconductor transitions.

Supplementary S6 – Id Characteristics

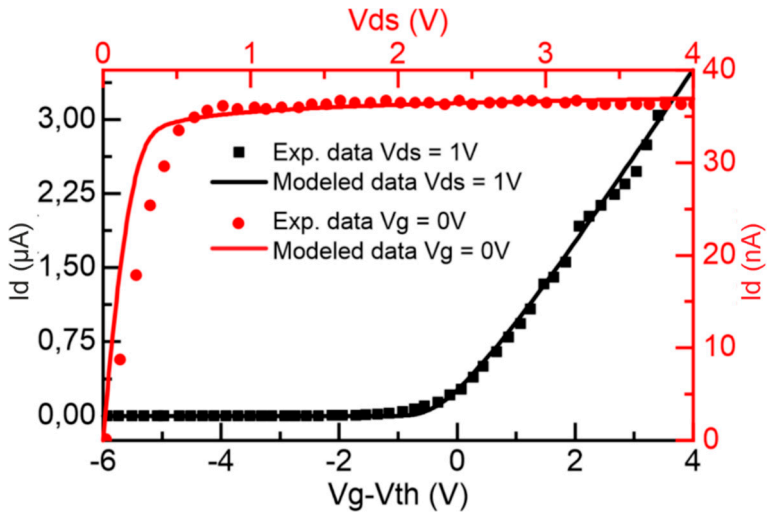


Figure S6. Plots of *Id(Vg-Vth)* and *Id(Vds).* Solid lines represent modeled data, while circles and squares correspond to experimental data from [Woong Choi, Advanced Materials, 2012], presented in both linear and logarithmic scales.

Figure S6 shows both experimental and simulated drain current (*Id*) dependencies for a field-effect transistor under two different operating modes: (1) *Id* versus *(Vg−Vth)* at a fixed drain-source voltage, and (2) *Id* versus *Vds* at a fixed gate voltage. In the *(Vg−Vth)* mode, the experimental data (black squares) exhibit good agreement with the modeled results (black line). For positive values of *(Vg−Vth)*, *Ids* increases linearly, indicating that channel inversion is the dominant effect under charge-accumulation conditions. This close match between the experiment and the model confirms the accuracy of the chosen parameters in this voltage range. However, in the *(Vds)* mode, the experimental data (red circles) deviate from the simulated values (red line) at lower currents; specifically, the experimental *Id* increases more gradually than predicted by the model. Possible reasons for these discrepancies include inhomogeneities in the actual thin film, such as crystalline defects or localized charge traps that affect current conduction, as well as simplifications in the model itself, which may not capture certain complex effects associated with surface or thin-film states. Additionally, thin-film phenomena like surface roughness, interfacial states, and variations in film thickness can introduce further differences between the simulated and experimental results. Despite these deviations, the overall consistency across most bias ranges confirms that the model adequately captures the primary transport mechanisms and is a valuable tool for simulating quasi-2D field-effect transistors.

Supplementary S7 - Charge Carrier Concentration in the MoS_2 Film

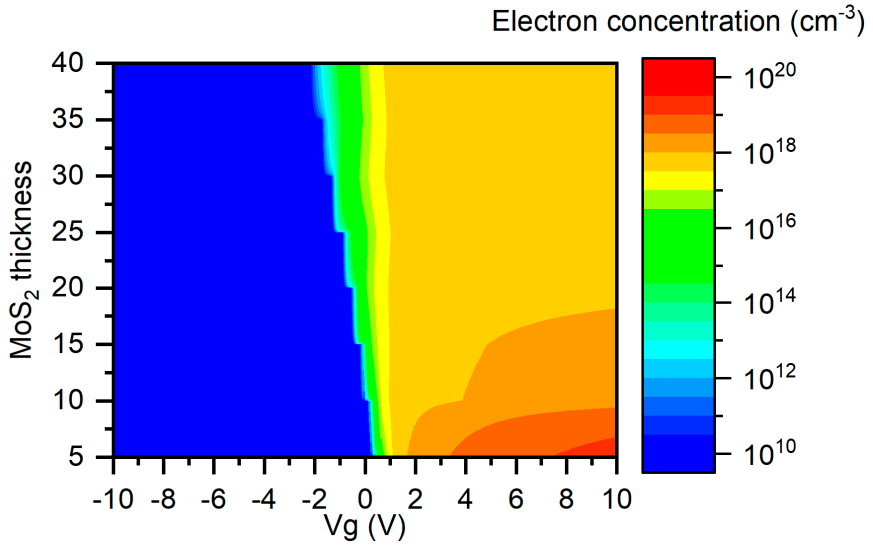


Figure S7. Calculated diagram of electron concentration at the midpoint of the semiconductor channel in the phototransistor

This figure presents a calculated diagram of electron concentration at the midpoint of the semiconductor channel in the phototransistor. The diagram shows the dependence of electron concentration on channel thickness and gate voltage. A clear channel blocking line is observed, where the electron concentration decreases from 10^{18} cm^{-3} to 10^{10} cm^{-3}. Thicker channels exhibit higher baseline electron concentrations due to increased carrier mobility and density, which contributes to the overall conductivity of the channel.

The drain-source voltage (V_{ds}) is set to 2 V, consistent with the conditions depicted in Figure 3 of the main article.

Supplementary S8 - Influence of MoS_2 Thickness on Current

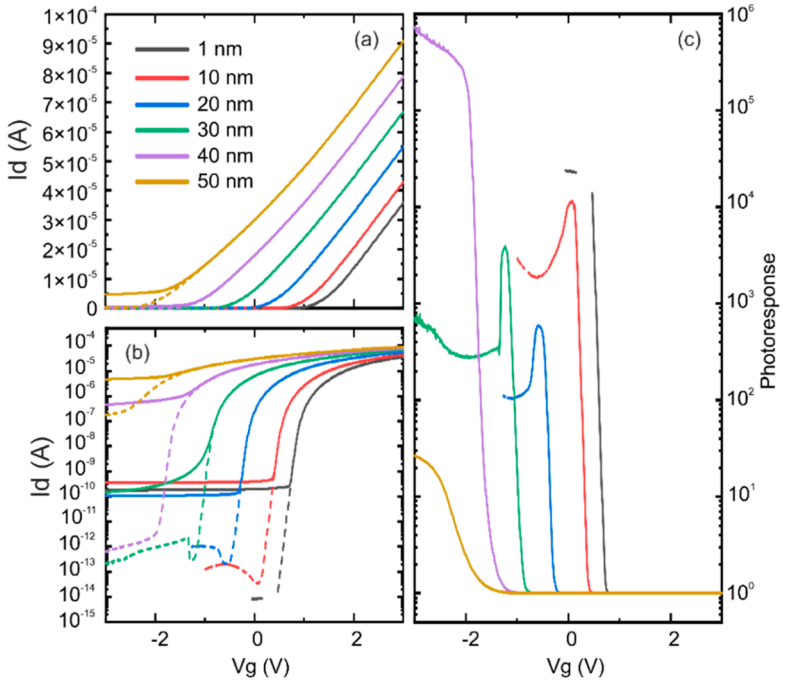


Figure S8. (a) Id-Vg dependence for photocurrent (solid lines) and dark current (dotted lines) for different channel thicknesses in linear scale. (b) Id-Vg dependence in logarithmic scale for different channel thicknesses. (c) Switching ratio as a function of channel thickness.

The figure S8a presents the I_d-V_g dependence in both linear and logarithmic scales for different channel thicknesses. The graphs qualitatively and quantitatively replicate each other, with differences primarily manifesting as linear shifts. This indicates that an increase in channel thickness leads to an increase in gate capacitance, which subsequently reduces the effective gate voltage.

This phenomenon is attributed to the redistribution of the electric field in the "gate-channel" system, where a thicker channel screens the gate's influence on charge carriers. To determine the threshold voltages (V_{th}) associated with transistor activation (as shown in the inset of Figure 3 in the main article), the linear regions of the curves were extrapolated to intersect the V_g-axis. The intersection point represents Vth, which corresponds to the onset of channel conductivity. Physically, this reflects the formation of an inversion layer of charge carriers sufficient to sustain current flow through the channel.

The increase in film thickness shifts V_{th}, which can be explained by changes in the potential distribution along the channel and the impact of geometry on charge injection characteristics. These findings emphasize the role of channel thickness in modulating the device's electrical properties, providing insights into optimizing transistor performance.

Figure S8b illustrates the dark current behavior for different channel thicknesses. As the thickness increases, there is a notable rise in the dark current, particularly in the pinch-off region (Vg << Vth). This increase can be attributed to the larger volume of the semiconductor available for current conduction and the reduced effectiveness of the gate in fully depleting thicker channels.

The switching ratio, defined as the ratio of photocurrent to dark current, is presented in Figure S8c for various channel thicknesses. Thinner MoS_2 layers exhibit superior switching

ratios, especially in the pinch-off regime. This enhanced performance in thinner films is due to their lower dark current, which allows for a greater contrast between the "on" and "off" states of the phototransistor. The improved switching characteristics of thinner films highlight the critical role of channel thickness in optimizing device performance, particularly for applications requiring high sensitivity and low dark current.

These results underscore the importance of carefully considering channel thickness in the design of MoS_2-based phototransistors. While thicker channels may offer higher overall current levels, thinner channels provide better switching performance and potentially higher sensitivity in photodetection applications.

Supplementary S9 - Assessment of the Depletion Region in MoS_2

This section presents cross-sectional profiles of the concentration of charge carriers (electrons, Fig. S9.1) along the entire length of the MoS_2 film and the potential distribution (Fig. S9.2). These results allow for an estimation of the depth of the depletion region, which, based on the figures, is approximately 50 nm for Vg =−2 V. As expected, the depletion depth increases with further decreases in gate voltage, reflecting the enhanced electric field influence.

At this gate voltage, the potential across the surface of the TMD film remains constant, except within the depletion region, where the charge carrier density is significantly suppressed. This isolates the active conducting channel. These profiles were obtained under a drain-source voltage (V_{ds}=2V).

These results are consistent with experimental observations of depletion depths in MoS_2 films under similar gating conditions. The depletion region plays a critical role in defining the switching characteristics and overall performance of the phototransistor, particularly under pinch-off conditions.

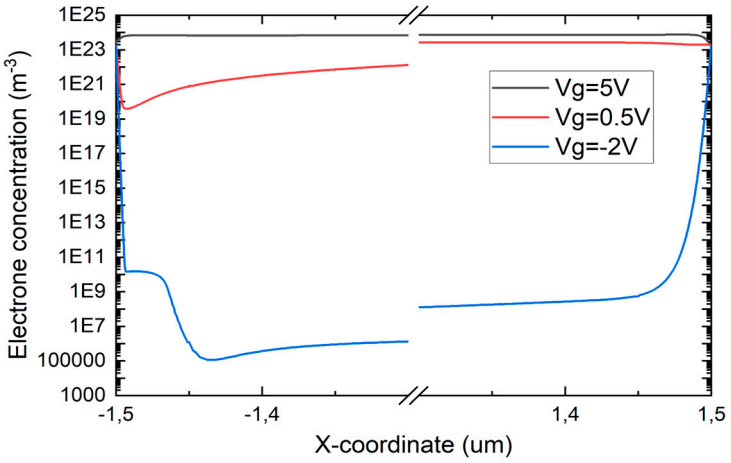


Figure S9.1. Cross-sectional profile of electron concentration along the length of the MoS_2 film at Vg=−2V and Vds=2 V.

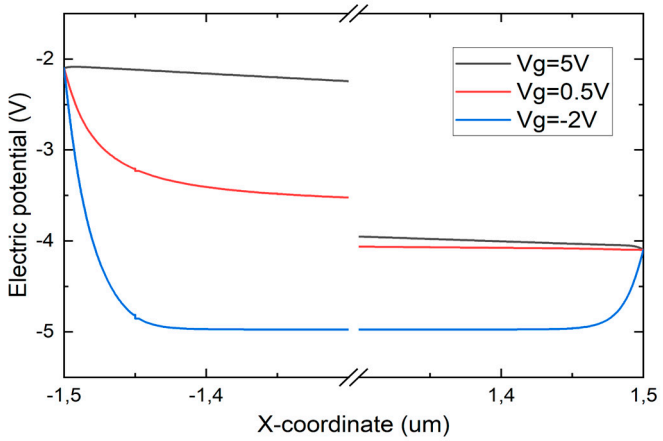
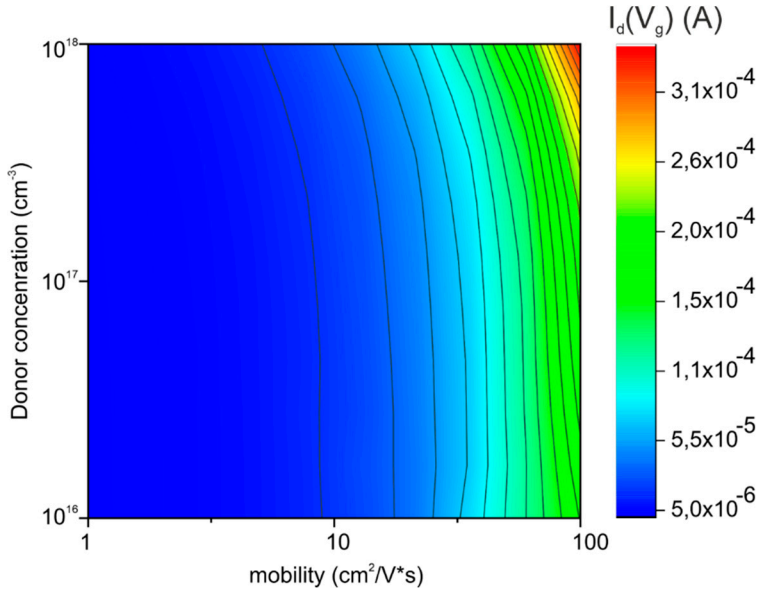


Figure S9.2. Potential distribution across the MoS_2 film at Vg=−2V and Vds=2 V.

Supplementary S10 - Dependence of Dark Current on MoS_2 Characteristics



S10. Dependence of dark current on donor concentration in the semiconductor channel and charge carrier mobility

The diagrams above depict the dependence of dark current (Ids) on donor concentration in the semiconductor channel and charge carrier mobility for V_d=1V and V_g=3V, corresponding to Figure 4 in the main article. The analysis reveals that donor concentration has a relatively minor effect on Ids, while charge carrier mobility emerges as the dominant factor. As mobility increases, Id rises significantly.

This phenomenon can be attributed to the direct relationship between mobility and the drift velocity of carriers under an electric field, whereas the influence of donor concentration is limited to its contribution to the overall conductivity of the channel. Parameters such as donor concentration and carrier mobility can vary widely depending on the fabrication method and the presence of defects or traps. In this study, the selected ranges for donor concentration and carrier mobility encompass all possible values for this material.

These findings emphasize the critical role of the film fabrication method in determining its operational characteristics. Accounting for these factors is essential when designing devices to optimize their performance.

Supplementary S11 - The impact of temperature on photocurrent behavior

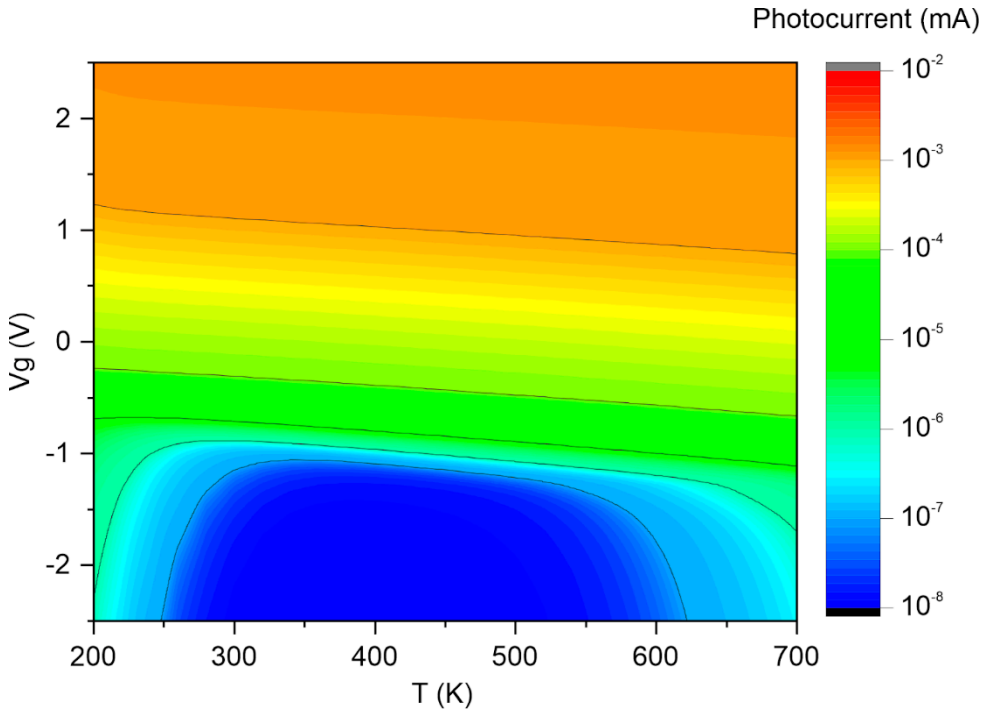


Figure S11. Dependence of Photocurrent (Logarithmic Scale) on Temperature and Gate Voltage.

As shown in the graph above, the photocurrent in the transistor's pinch-off regime (Vg << Vth) exhibits a strongly non-linear dependence on temperature. Specifically, at approximately room temperature (300K), the current is around 1e-8 mA, whereas increasing or decreasing the temperature causes the current to rise to 1e-7 or 1e-6 mA, respectively. In contrast, in the open gate regime (Vg >> Vth), the channel current remains relatively constant within the examined temperature range.

This behavior is due to competing physical mechanisms governing charge carrier transport in the pinch-off and conducting states. Two primary processes play a key role in shaping the temperature dependence of the current in the pinch-off regime: thermionic emission and quantum mechanical tunneling through the potential barrier. Our model accounts for all of these mechanisms.

In the pinch-off regime, the source-drain current is limited by the energy barrier formed at the metal-semiconductor contact. In this case, there are two main mechanisms for carrier transport across the barrier: thermionic emission, where electrons (or holes) overcome the barrier through thermal energy, and tunneling, where carriers have a finite probability of passing through the potential barrier without overcoming it.

At temperatures above room temperature, thermionic emission dominates. Increasing the temperature leads to a higher number of carriers with sufficient energy to surmount the barrier, thus increasing the current. This effect is most pronounced in the pinch-off regime, as the current is mainly determined by carrier generation and transport through the barrier rather than their transport within the channel.

When the temperature decreases below room temperature, the contribution of thermionic emission weakens as the probability of overcoming the barrier exponentially decreases. However, the tunneling mechanism simultaneously becomes more significant. In the quantum mechanical approximation, the probability of carriers tunneling through the potential barrier is described by the Wentzel-Kramers-Brillouin (WKB) model. As a result, the tunneling contribution increases as the temperature drops, leading to an increase in the current in the pinch-off state.

A fundamentally different behavior is observed in the conducting channel regime (Vg >> Vth). In this regime, the concentration of free carriers in the channel significantly exceeds the thermally induced concentrations, and their movement is primarily determined by drift and diffusion under the influence of the electric field. The main contribution to the current comes from Ohm's law and diffusion processes. Since the majority of carriers in this regime are already induced by the electrostatic field of the gate, the effect of thermionic emission and tunneling on the total current is insignificant. Moreover, thermionic emission, which is the dominant mechanism in the pinch-off region, does not play a significant role in the open state because the gate potential effectively reduces the energy barrier, allowing free transfer of carriers between the contact and the channel. Similarly, tunneling does not have a significant impact because the potential in the channel already allows carriers to move freely, eliminating the need for their quantum mechanical penetration through the potential barrier.

Supplementary S12 - The impact of optical power on photocurrent behavior

To investigate carrier behavior in low-light environments using the proposed field-effect transistor model, photocurrent transfer characteristics Id(Vg) were simulated at various incident radiation powers (with Vd=1V). The simulation results are presented in Figure S12. The pump radiation wavelength was set at 633 nm.

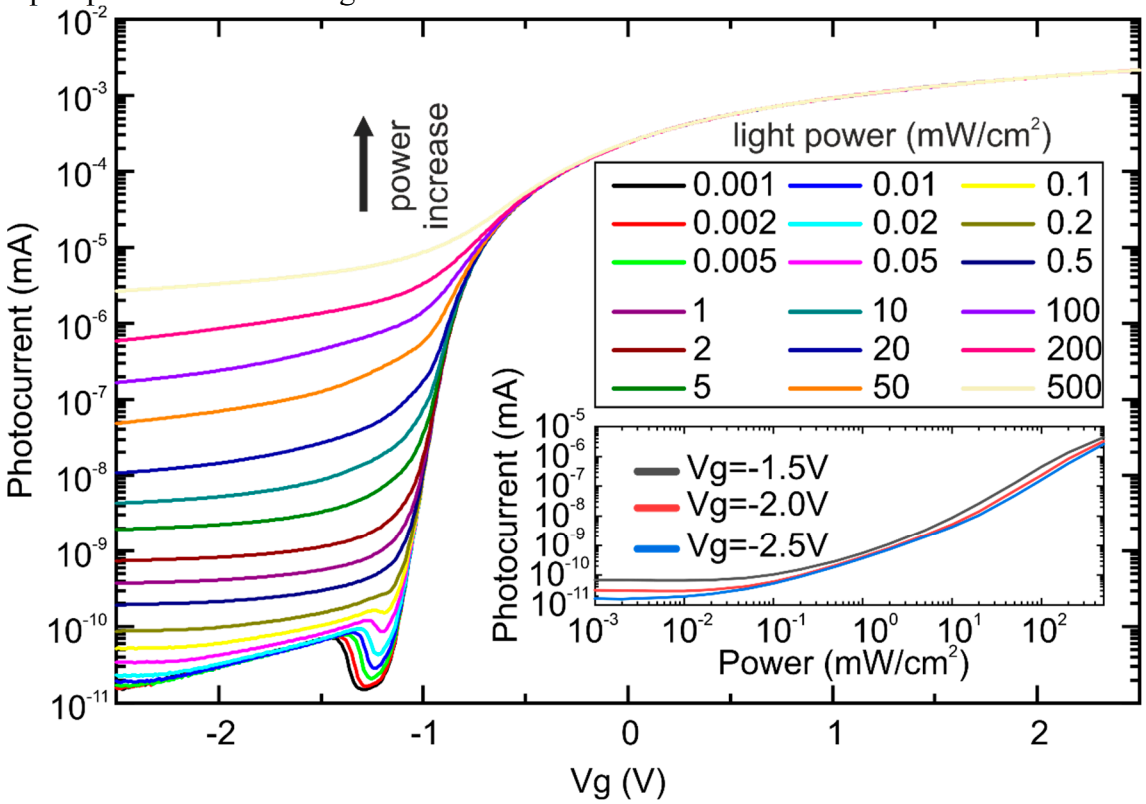


Figure S12. Dependence of photocurrent on gate voltage at different optical radiation power densities. The inset shows the photoresponse as a function of incident power density. The optical radiation wavelength was chosen to be 633 nm.

The obtained graphs can be divided into two distinct regions with markedly different dependencies. The threshold value is approximately Vg = -0.5 V.

The simulations reveal that at higher gate voltages (Vg > -0.5 V), the photocurrent becomes independent of the incident power, and the dark current significantly outweighs the photocurrent, thus rendering the device insensitive to incident light. However, at lower gate voltages, the photodetector exhibits a strong sensitivity to the incident light, confirming that operating in the pinch-off region indeed optimizes the photodetector's response.

Despite their highly non-linear nature, the obtained power dependence curves are standard for photodetectors based on two-dimensional semiconductors, as corroborated by literature data [R.Nur, Commun Mater, 2020; H.Park, Commun Mater, 2021].

From these results, we can determine the threshold sensitivity of the modeled sensor. In this case, it is approximately 50 nW/cm², which can be derived from the power dependence presented in the inset of Figure S12.

Supplementary S13 - The impact of electrode materials

To investigate how electrode materials affect photocurrent behavior we have performed additional simulations for the most common electrode materials, with results presented on figure S13. The main parameters used in these simulations are provided in the accompanying table. The results clearly show that changing the electrode material affects the threshold voltage (Vth) position and the final current value in the positive Vg (right part of the graphs). However, in the pinch off conditions (left part of the graphs), the contribution of the electrode material is minimal, with the obtained dependencies converging to a common curve.

From these results, we conclude that the choice of electrode material does not significantly affect the final performance of the photosensor when operating in the pinch-off mode. This finding is particularly relevant for optimizing device sensitivity while minimizing the impact of electrode material variations.

Electrode material	Barrier height (eV)	Refference
Sc	0.030	10.1021/nl303583v
Ti	0.100	10.1021/acsnano.0c02303
Ni	0.150	10.1021/nl303583v
Au	0.126	10.1063/1.4895767
Pd	0.250	10.1021/nn406603h
Pt	0.230	10.1021/nl303583v

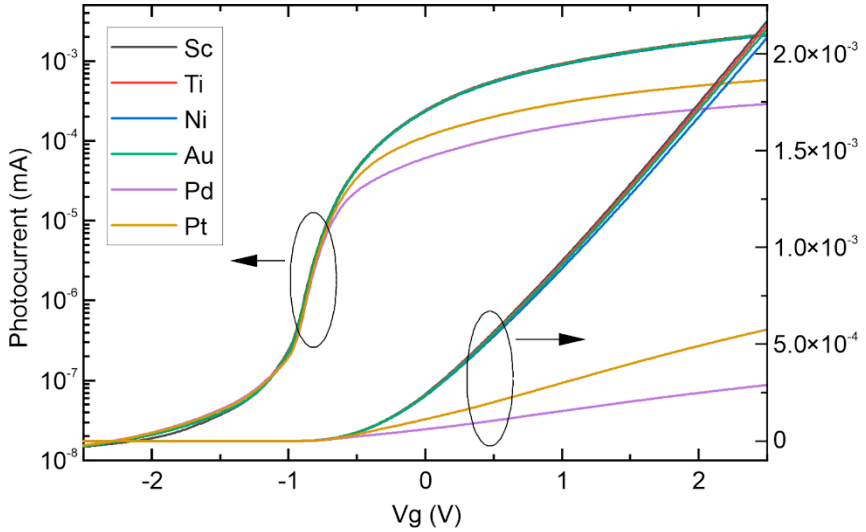


Figure S13. Dependence of photocurrent on gate voltage for different electrode materials, shown in both linear and logarithmic scales.